Original Article

Three Phase Induction Motor for Marine Propulsion System Using Nature Inspired Algorithm Based ANFIS Controller with 31 Level CHB MLI

R.K. Padmashini[1], D. Lakshmi[2], V. Pramila[3], J.N. Rajesh kumar[4]

[1,2]Department of Electrical and Electronics Engineering, AMET Deemed to be University, Tamilnadu, India.
[3]Department of Electrical and Electronics Engineering, B.S. Abdur Rahman Institute of Science and Technology, Tamilnadu, India.
[4]Department of Computer Science Engineering, Sree Sastha Institute of Engineering and Technology, Tamilnadu, India.

[1]Corresponding Author : padmashnirk12@yahoo.com

Abstract - This work proposes a 31 level Cascaded H Bridge Multi Level Inverter (CHB MLI) with an optimized Adaptive Neuro Fuzzy Interference System (ANFIS) controller to regulate a three phase Induction Motor (IM) drive for a marine propulsion system. Here, using affordable Renewable Energy Sources (RES) is the most effective option to satisfy the desired energy demand. To compensate for one's shortcomings with another's strengths, this research uses Photovoltaic (PV) and Doubly Fed Induction Generator based Wind Energy Conversion Systems (DFIG-WECS) as power generation sources. High gain Single Ended Primary Inductance Converter (SEPIC) is used in the work under consideration to boost PV voltage, and Lion Algorithm optimised ANFIS (LA-ANFIS) is used for efficient converter regulation. Additionally, to ensure efficient control, the AC supply from DFIG-WECS is converted to DC employing a PWM rectifier and LA-ANFIS controller. A 31 level Cascaded H Bridge Multi Level Inverter (CHB MLI) is used in the marine propulsion systems to convert the converter's output into distortion-free alternating current voltage fed to the motor. Utilizing a PI controller, the three-phase IM speed is controlled, producing outcomes with regulated speed. The overall proposed system was verified using the MATLAB platform, and the results prove that the proposed method is more efficient than other existing approaches.

Keywords - PV, DFIG-WECS, Lion optimized ANFIS controller, High gain SEPIC, IM, 31 level CHB MLI.

1. Introduction

The marine propulsion sector has become more involved in hybrid technology as there is a growing need to build more sustainable and effective ships. The last several years have seen several advancements in hybrid marine propulsion because of the innovation in battery technology, which provides the adaptability of picking energy sources. Hybrid propellers are used in the marine industry to reduce carbon emissions and direct the industry towards zero emissions. By lowering reliance on traditional fossil fuels, the Renewable Energy Source (RES) is utilized, and the greenhouse gas emissions caused by fossil fuels are decreased [1]. In recent years, PV and WECS have become increasingly popular as renewable energy sources for power systems. The WECS and PV energy are inherently unstable and weather-dependent. In these situations, combining wind and solar energy simultaneously rather than focusing on a single energy source (wind energy or solar energy) results in a more efficient and dependable system [2, 3]. Hybrid Renewable Energy Systems (HRES) combine two or more renewable energies to produce electricity [4]. Innovations in renewable energy technologies have led to hybrid renewable energy systems becoming more widely used in electricity production.

Continuous power delivery to localized loads requires WECS and PV systems to be accessible with extra energy storage systems. In this instance, the energy storage device is a battery bank [5, 6]. On ships and submarines, induction motors are primarily used for additional machinery. Due to recent advancements in power electronics, induction motor controls are employed for various speeds with a quick dynamic response [7].

The literature presents a variety of control technique designs for marine propulsion systems. It has been suggested in [8, 9] to implement simplified space vector PMW in modular multilevel converters for electrical marine propulsion systems. Considering conditions of speed change, rapid velocity, and stable state, the proposed method

performs better. Synchronizing the carriers is difficult for an MMC with many SMs because of storage limitations and computation interruptions. The modified SVM approach is proposed in [10] as a diagnostic and health-tracking strategy for marine propulsion systems. The updated SVM achieves quantitative defect detection performance. However, compared to the initial signal, a single residual vector norm holds far less data. A PV/diesel/storage hybrid electrical system for commercial marine vessels is proposed in [11] using stochastic-based risk-constrained optimum sizing.

The CVaR methodology effectively quantifies the risk associated with the size issue. However, the effects of the best battery sizing on the system's viability are not considered. In [12, 13], driven by data resilient production and demand-side management in PV-incorporated all-electric ship microgrids have been suggested. Propulsion load control on the demand side provides versatility for PV adoption. However, several distinctions from load-based systems need to be made in the shipboard PV forecasting due to the unique nature of the "mobile microgrid".

In [14], it had been suggested the hybrid photovoltaic/battery/diesel generator design be used for maritime electrical systems. The PSO application determines the ideal ESS and PV size. However, improvements must be made to the proposed system for high-speed trains and container ships. The MVDC shipboard has integrated storage and capacitive and resistive droop controllers: An optimum flow approach has been proposed in [15, 16].

The results support the proposed formulation's effectiveness in managing the energy between storage units and supporting load. But shipboard power systems rarely employ this control level. In [17], stochastic dynamical properties of marine rotor-bearing systems under heaving motion are proposed. This system demonstrates how heave motion significantly affects the systems' dynamic behaviours.

Nonetheless, the system's steady-state response displacement gradually decreases before increasing. Therefore, this work proposes an efficient control approach to tackle the abovementioned challenges. The main contribution of this work is summarized as follows:

➢ To operate an IM with a combination of solar and wind energy systems.
➢ Improved efficiency with fewer transition losses is obtained using a high-gain SEPIC converter.
➢ The development of an optimized controller maintains constant dc link voltage with enhanced dynamic response.

➢ Using the Battery Energy Storage (BES) technology, it is possible to effectively preserve the power flow balance while storing the excess energy from hybrid systems.
➢ To utilize the 31 Level CHB MLI to efficiently convert the appropriate DC to AC voltages with a minimal THD.
➢ To leverage the PI controller to manipulate the speed of the IM motor.

In the remainder of the article, the structure is as follows. The proposed system is described in Section 2, and its mathematical modelling is covered in Section 3. Discussions and outcomes from simulations are presented in Section 4. In Section 5, the paper is concluded.

2. Proposed System Description

Hybrid propulsion systems are used in the maritime sector to reduce greenhouse gases and drive the industry into emission-free operation. By lowering the dependability of imported traditional fossil fuels, the RES is utilized, and the production of greenhouse gases caused by fossil fuel consumption is lessened.

Therefore, this paper proposes employing a three-phase induction motor supported by a combination of solar and wind energy for the marine propulsion system. Figure 1 illustrates a schematic representation of the proposed work.

At the distribution level, power is produced using sustainable clean energy. A high-gain SEPIC converter is positioned across the inverter and the PV panel to boost and stabilize the DC voltage coming from the solar panel. Adjusting its duty cycle D, a high-gain SEPIC converter provides the common coupling point with a constant voltage.

The Lion-optimized ANFIS controller is implemented to stabilize a converter voltage since the output of a converter is unreliable and frequently fluctuates because of the inconsistent characteristics of the PV radiation. The signal that indicates an error is obtained from comparing the converters' actual DC voltage output to the reference voltage of a Lion-optimized ANFIS controller. The PWM generator derives PWM pulses from a control signal the controller provides.

The signals produced by pulses govern the converter's transitioning operation to deliver a consistent result. Energy from the WECS-based DFIG is supplied as Alternating Current (AC), which the PWM rectifier converts to Direct Current (DC). As the WECS' output power changes with the variance in wind velocity, the Lion-optimized ANFIS controller stabilizes the voltage generated from the PWM rectifier.
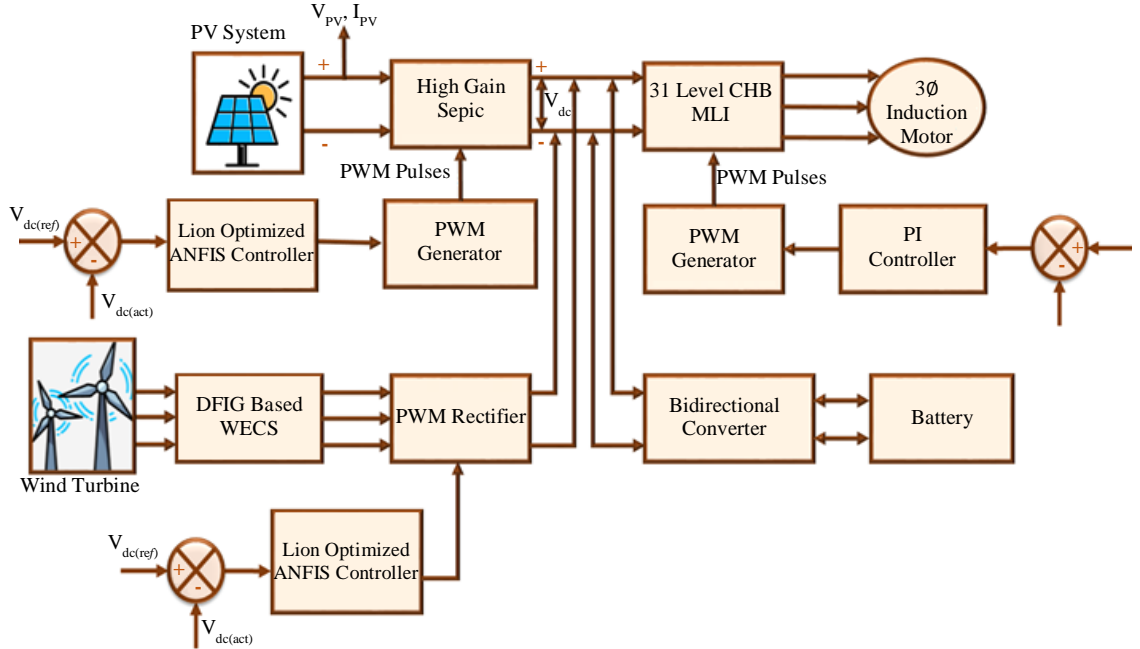
Fig. 1 PV-wind powered three-phase induction motor using 31-level CHB MLI

Battery energy is released to sustain the voltage whenever the PV power cannot supply electricity to the loads. The battery is charged and discharged according to the load's requirements by a bidirectional DC-DC converter. The DC voltage obtained from the converter is converted into AC voltage by the 31 level CHB MLI, which is adequate for the three-phase Induction motor IM to operate efficiently. The PI controller governs the three-phase induction motor to function at a desirable speed.

3. Proposed System Modelling
3.1. PV System Modelling

In broad terms, solar panels transform sunlight into electrical power. A cell is an individual PV device. The PV cells are placed in series and parallel to form a solar panel. The amount of series and parallel cells determines the current as well as voltage of the PV panel. Since PV arrays are asymmetrical devices, the comparable circuitry model, depicted in Figure 2(a), is widely used to trigger their characteristics.

The basic formula for a PV panel is as follows:

$$I_{pv} = I_{sh} - I_d - I_p \qquad (1)$$

I_d is the amount of current passing via the diode and I_p is the current flowing through the resistance parallel to the circuit, and these values are provided in Equations (2) and (3) correspondingly.

$$I_d = I_O \left[\exp\left(V + \frac{IR_S}{aV_T} \right) - 1 \right] \qquad (2)$$

$$I_p = \left(V + \frac{IR_S}{R_p} \right) \qquad (3)$$

By combining Equations (2) and (3), the following equation is obtained:

$$I_{pv} = I_{sh} - I_O \left[\exp\left(V + \frac{IR_S}{aV_T} \right) - 1 \right] - \left(V + \frac{IR_S}{R_p} \right) \qquad (4)$$
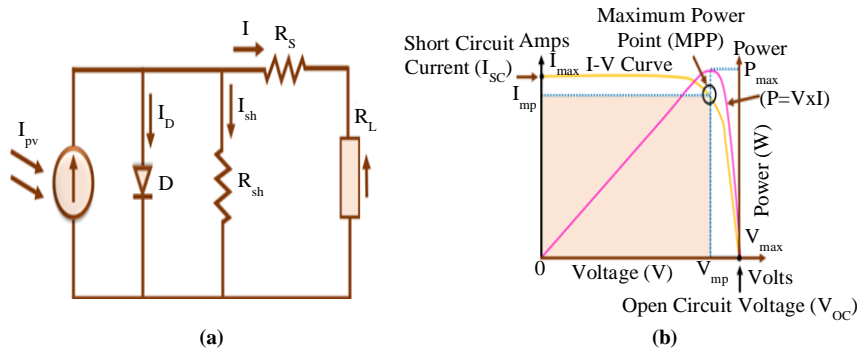

(a)   **(b)**
Fig. 2 PV panel modelling (a) Equivalent circuitry, and (b) Characteristics of PV.

At every stage of testing conditions, I-V and P-V curves can be calculated from the entire representative equation of the solar panel model, Equation (4), which includes the independent variables. PV panel properties tend to be determined by IV and PV curves, as illustrated in Figure 2(b). The appropriate converter is used to control the constant voltage that comes from the solar energy system. This work employs a High-gain SEPIC converter, which is discussed below.

3.2. Modelling of High Gain SEPIC Converter

A high-gain SEPIC for applications involving high voltages is proven in the current work. A conventional SEPIC was modified to yield the converter under consideration, which has a single input-output port. The high gain SEPIC power circuit is shown in Figure 3(a) and consists of three capacitors (C_a, C_b, and C_o) inductors (L_a, L_b, and L_c) and diodes (D_a, D_b, and D_c), all of which are controlled by a single switch (S). The High gain SEPIC converter uses an inductor. L_b and a capacitor C_a as voltage-boosting components in addition to two diodes.

The complete system has to be preferable, and all capacitors must be more significant to preserve a consistent voltage and depict a state of equilibrium operating. As shown in Figures 3(b) and 3(c), the converter is controlled by a switch S, which causes it to operate in two stages: phase-I (t_0 to t_1) and phase II (t_1 to t_2). Where $T_s=1/f_s$ denotes the time required to complete one switching cycle, and k stands for the duty factor.

3.2.1. Phase I: (t_0 to t_1)

Three inductors are handled in phase- I using each of the following present paths: inductance L_a from the electrical source (V_{in}-V_{La}-D_b-S-V_{in}), inductor L_b from the capacitor C_a (V_{ca}-V_{Lb}-S-V_{ca}), and inductor L_c from the capacitor C_b. According to Figure 3(b), capacitor C_o reverse biased the diode D_c at the exact right time, transferring electricity to the load.

$$Phase\ I = \begin{cases} V_{La} - V_{in} \\ V_{Lb} - V_{cb} \\ V_{Lc} - V_{co} \end{cases} \qquad (5)$$

Here V_{La}, V_{Lb} and V_{Lc} denote the voltages that pass through inductors L_x, L_y, and L_z, correspondingly. The voltage over the capacitors C_1, C_2 is represented by V_{c1}, V_{c2}.

3.2.2. Phase II: (t_1 to t_2)

All three inductors are demagnetized in the following manner in phase II: The supplied voltage (V_{in}-V_{La}-D_a-C_a-V_{in}) imposes the capacitor C_a through the inductor L_a. The circuit (V_{ca}-V_{Lb}-V_{cb}-D_c-V_o-V_{ca}) charges capacitor C_b through the configuration of an inductor L_b and capacitor C_a. Inductor L_c conducts simultaneously through the load using the V_{Lc}-D_c-V_o pathway shown in Figure 3(c).
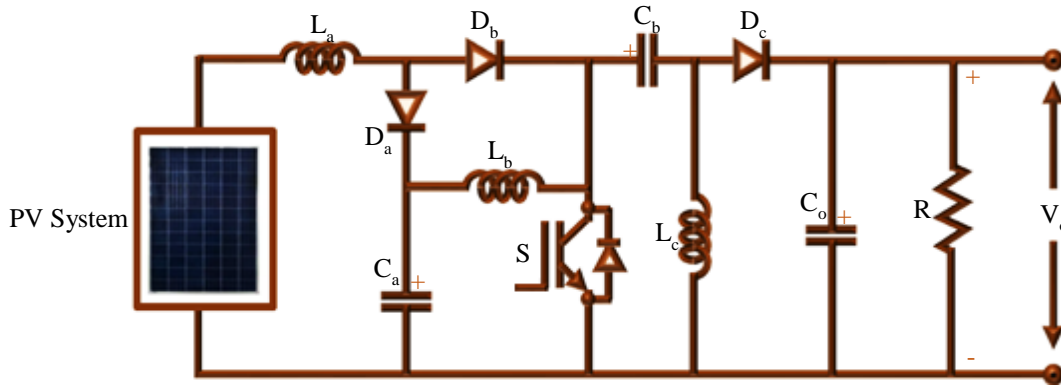

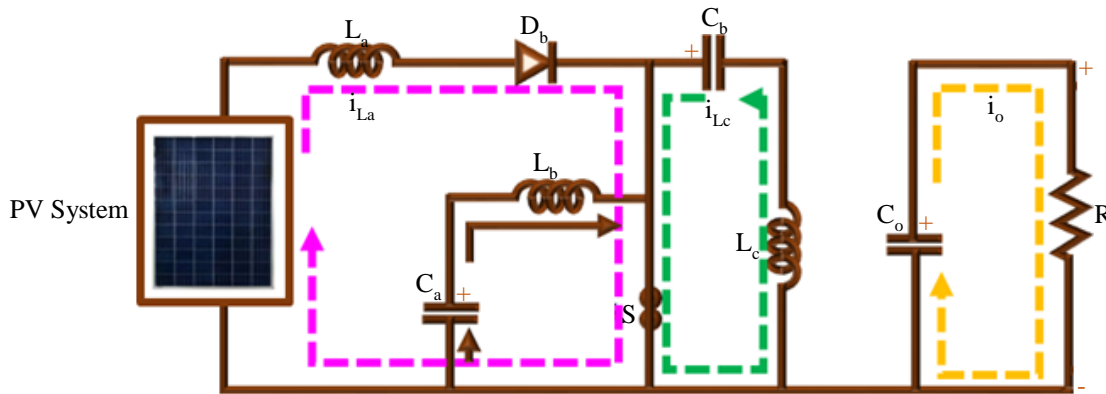**Fig. 3(a) High-gain SEPIC converter**
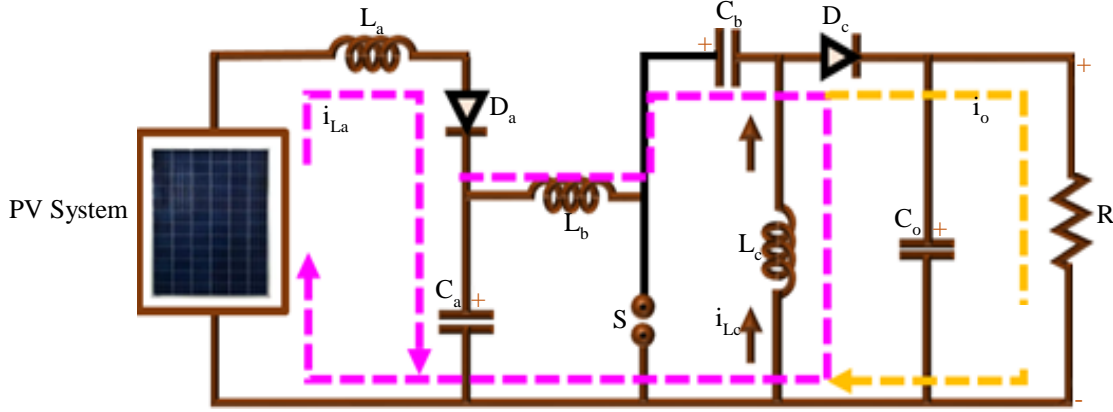

Fig. 3(b) Phase I
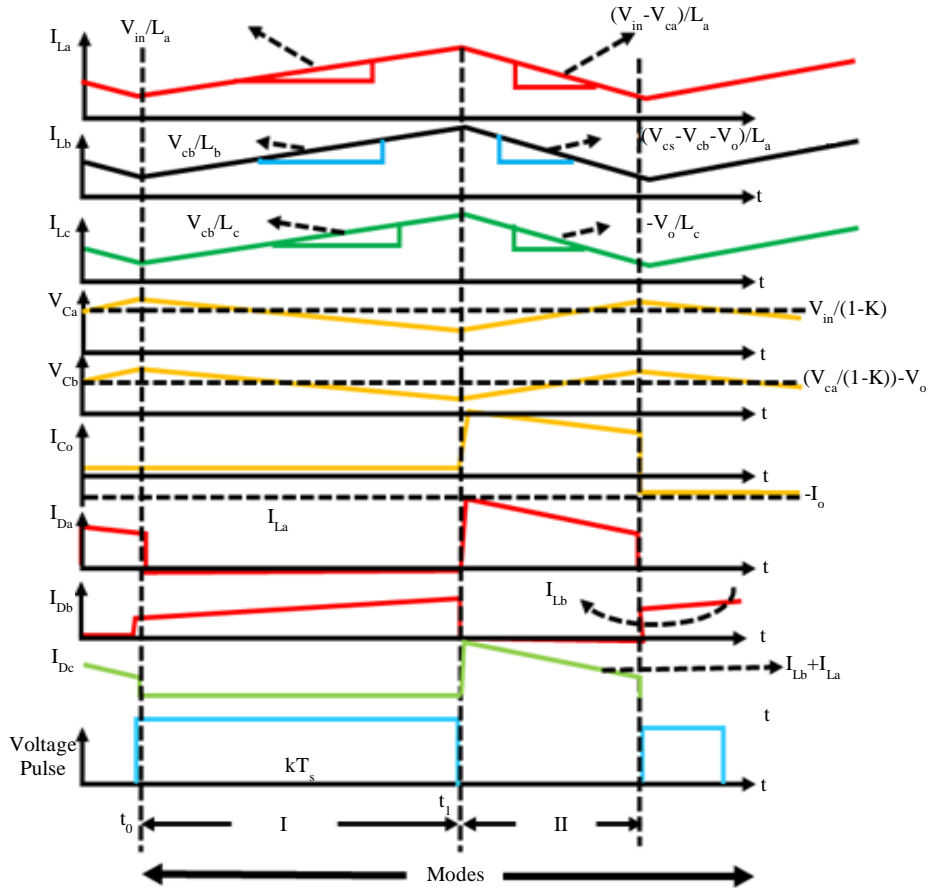
Fig. 3(c) Phase II

Fig. 4 The conceptual waveform of the proposed converter

The waveform configuration representing the proposed converter operating modes is shown in Figure 4. The proposed High-gain SEPIC has numerous advantages, such as lower switching losses, constant input current flow, and high voltage gain.

3.3. WECS Modelling
3.3.1. Wind Turbine Model
A Wind Turbine (WT) converts the wind's kinetic energy into rotating energy.

$$P_v = \frac{1}{2}\rho A V_v^3 \tag{6}$$

Where, A indicates the area covered by turbine blades (m2), r is the air volume (kg/m3), and V_v is the wind velocity (m/s). Equation (7) provides the power that the turbine draws from the available wind energy:

$$P_t = \frac{1}{2}\rho\pi R^2 V_v^3 C_p(\lambda, \beta) \tag{7}$$

Where, R is the radius of the turbine rotor (m) and $C_p(\lambda, \beta)$ is the coefficient of performance. The power coefficient and C_p are affected by tip speed ratio (l) and pitch angle (b).

Equation (8) gives the torque produced by the turbine.

$$T_t = \frac{P_t}{\omega_t} \tag{8}$$

3.3.2. DFIG Model

Windings are on both the stator and rotor make up the DFIG. A three-phase transformer connects the stator to the grid through three-phase isolated windings surrounding the slide rings. As with the stator, the rotor is also made up of three-phase isolated windings. The rotor windings are connected to the fixed circuit outside through slipping rings and brushes. The rotor windings are either injected into or absorbed from these parts to regulate rotor current.

The fluctuating DFIG model is represented using a combination of direct and opposite transformations. According to the space vector concept, the two stationary windings $\alpha\beta$ for the stator and the spinning winding dq for the rotor can represent the three windings of the rotor and stator. The voltage vector of the stator and rotor is written as:

$$\vec{u}_s \Rightarrow \begin{cases} u_{ds} = R_s i_{ds} + \frac{d\psi_{ds}}{dt} - \omega_s \psi_{qs} \\ u_{qs} = R_s i_{qs} + \frac{d\psi_{ds}}{dt} - \omega_s \psi_{ds} \end{cases} \tag{9}$$

$$\vec{u}_s \Rightarrow \begin{cases} u_{dr} = R_r i_{dr} + \frac{d\psi_{dr}}{dt} - \omega_r \psi_{qr} \\ u_{qr} = R_r i_{qr} + \frac{d\psi_{ds}}{dt} - \omega_r \psi_{dr} \end{cases} \tag{10}$$

Where, the rotor and stator voltages in the dq frame are denoted by the symbols u_{qs}, u_{ds}, u_{dr}, and u_{qr} correspondingly. Stator and rotor current in the dq frame are denoted, accordingly, by the symbols i_{ds}, i_{qs}, i_{dr}, and i_{qr}. Phase resistance for the stator, rotor, winding speed, and winding are denoted as R_r, R_s, ω_s, and ω_r. Figure 5 illustrates the dq comparable electric circuit derived from Equations (9) and (10).

Equations (11) and (12) are used, as well, to represent the flux vectors for the rotor and stator:

$$\vec{\psi}_s \Rightarrow \begin{cases} \psi_{ds} = L_s i_{ds} + L_m i_{dr} \\ \psi_{qs} = L_s i_{qs} + L_m i_{qr} \end{cases} \tag{11}$$

$$\vec{\psi}_r \Rightarrow \begin{cases} \psi_{dr} = L_m i_{ds} + L_r i_{dr} \\ \psi_{qr} = L_m i_{qs} + L_r i_{qr} \end{cases} \tag{12}$$

Where, the flux vectors for the stator and rotor are $\vec{\psi}_s$ and $\vec{\psi}_r$ respectively. The fluxes on the dq axis rotor are denoted by ψ_{dr} and ψ_{qr}. Together with the dq axis stator, the fluxes are ψ_{ds} and ψ_{qs}. L_s, L_r are the respective stator and rotor phase leakage inductances. L_m stands for stator-rotor mutual inductance, while p represents the generator's number of pole pairs.

Equation (13) contains the electromagnetic torque expression:

$$T_{em} \frac{3}{2} p \frac{L_m}{L_s} (\psi_{qs} i_{dr} - \psi_{ds} i_{qr}) \tag{13}$$

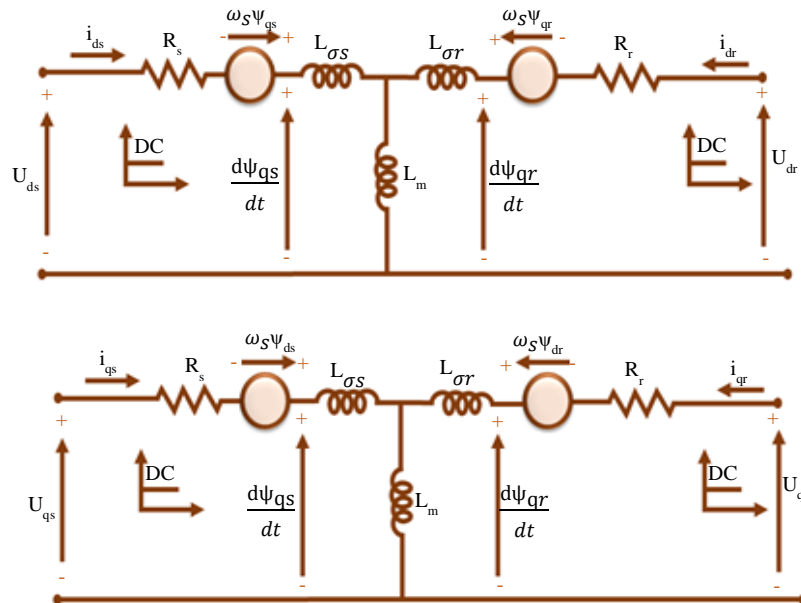Formulas (14) and (15) provide the stator and rotor's power reactive and active calculations.

Fig. 5 Equivalent circuit of DFIG

$$\begin{cases} P_s = \frac{3}{2}\left(u_{ds}i_{ds} + u_{qs}i_{qs}\right) \\ Q_s = \frac{3}{2}\left(u_{qs}i_{ds} - u_{ds}i_{qs}\right) \end{cases} \qquad (14)$$

$$\begin{cases} P_r = \frac{3}{2}\left(u_{dr}i_{dr} + u_{qr}i_{qr}\right) \\ Q_r = \frac{3}{2}\left(u_{qr}i_{dr} - u_{dr}i_{qr}\right) \end{cases} \qquad (15)$$

Where, P_s and Q_s are the active and reactive power of the stator, correspondingly. Rotor active and reactive power are shown, accordingly, in P_r, Q_r. The electromagnetic torque symbol is T_{em}.

Equation (16) expresses the basic torque expression:

$$T_{em} = T_{load} = J\frac{d\omega_m}{dt} \qquad (16)$$

J stands for the rotor's inertia, T_{load} for the load torque delivered to the shaft and ω_m for rotor speed.

3.4. Lion Optimized ANFIS Controller

This paper presents a Lion-optimized ANFIS controller for improving the operation of a hybrid PV-wind system. The Lion optimization method achieves a good equilibrium between exploration and exploitation; furthermore, this algorithm is utilized to fine-tune the parameters of the ANFIS controller to get better outcomes. The model findings reveal that the Lion-optimized ANFIS model controller has higher effectiveness and dynamic response, as detailed in the section below.

3.4.1. ANFIS Controller

Jang developed a hybrid approach named ANFIS in 1993, which combined the benefits of Artificial Neural Networks (ANN) and fuzzy logic into one structure. The Takagi-Sugeno inference approach, which employs fuzzy IF-THEN rules to construct a nonlinear relationship from input space to output, is used. ANFIS is made up of five layers, as shown in Figure 6.

If x and y are described as crisp inputs to node i, then the result of every node is specified in the first layer as,

$$O_{1i} = \mu_{Ai}(X), \quad i = 1,2 \qquad (17)$$

$$O_{1i} = \mu_{Bi-2}(Y), \quad i = 3,4 \qquad (18)$$

Where, Ai and Bi are the members of the function values $\mu_{Ai}(X)$ and $\mu_{Bi-2}(Y)$ Correspondingly. The subsequent generalized Gaussian function defines these values.

$$\mu_x = e^{\left(x-\frac{P_i}{x_i}\right)^2} \qquad (19)$$

Where, P_i and x_i are the data's standard deviation and mean, correspondingly. They are referred to as assumption conditions defined in the literature. In the subsequent layer, every node generates the firing intensity according to a specific rule:

$$O_{2i} = \mu_{Ai}(x) * \mu_{Bi-2}(y) \qquad (20)$$

The normalized firing intensity derived by the subsequent equation results from every node in the third layer.

$$O_{3i} = \overline{wi} = \frac{\omega_i}{\sum_{i=1}^{2}\omega_i} \qquad (21)$$

The fourth layer is made up of adaptable nodes, and each flexible node generates output based on the function:

$$O_{4,i} = \overline{w}_i fi = \overline{w}_i(P_i x + q_i y + r_i) \qquad (22)$$

Where, P_i, q_i and r_i are the ith adaptive node's subsequent variables. Lastly, the whole output is represented by one node in the fifth layer. The result is specified as follows:

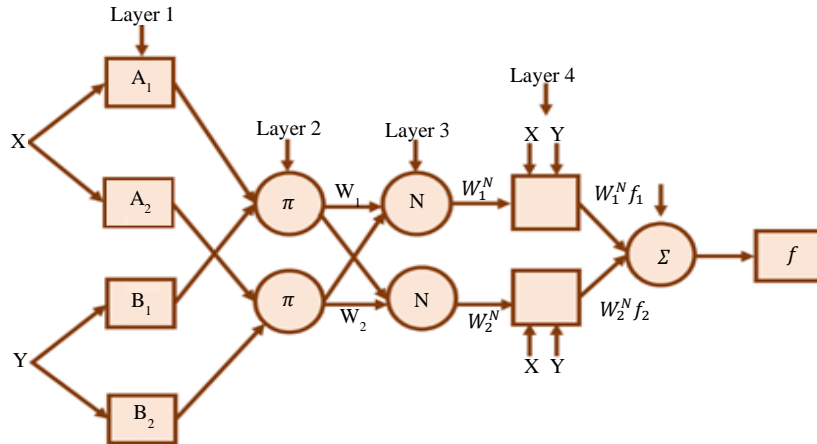$$O_5 = \sum_i \overline{w}_i fi \qquad (23)$$

Fig. 6 ANFIS structure

Adaptable factors such as assumption and consequence are critical in determining the efficacy of the ANFIS. In ANFIS, non-steady parameters cause problems. Some of the drawbacks of ANFIS are minimized by utilizing a Lion optimization algorithm.

3.4.2. Lion Optimization Algorithm

The LOA is constructed by employing lion behaviour patterns such as mating, hunting, and defending. Lions' behavioural organization is simultaneously resident and itinerant. Individuals form groups known as prides. Any lion, resident or nomad, can evolve. Each response has been referred to as a "Lion" in the LOA, whereby the first group is generated at randomized across a solution space.

A proposed LOA-based method is described as follows:

- Phase 1: To identify an approach to an issue using cloud computing and reduce the time necessary to accomplish a complete level.
- Phase 2: Every pride is going to do the following:

Step 2.1 - Hunting: On the assumption of LOA, an unplanned group of females from pride is selected for hunting. These predators approach and surround their victims to catch them. The selected female hunters are subsequently randomly separated into right, left, and centre wing groups.

The group exhibiting the most outstanding fitness rating is known as the centre, while the other two groups are known as the wings. Following that, prey is generated in the centre of the hunters, as illustrated below.

$$PREY = \frac{\sum hunters\ positions}{number\ of\ hunters} \quad (24)$$

Every hunter approaches the target based on the group to which it belongs. If a hunter belongs to the middle group:

$$Hunter' = \begin{cases} rand((Hunter)PREY).\ (Hunter) < PREY \\ rand(PREY.(Hunter)).(Huter) > PREY \end{cases} \quad (25)$$

Whether it belongs to the left or right wings:

$$Hunter' = \begin{cases} rand((2 \times PREY - Hunter)PREY) \\ ((2 \times PREY - Hunter) < PREY \\ rand((PREY.(2 \times PREY - Hunter) \\ (2 \times PREY - Hunter) > PREY \end{cases} \quad (26)$$

During hunting, if the individual's position is better than the prey's previous status, the target will flee and relocate to a new area, improving the hunter's abilities.

$$PREY' = PREY + rand(0.1) \times PI \times (PREY - Hunter) \quad (27)$$

Where, PI denotes an approximate improvement in hunter fitness.

Step 2.2 - Remaining Females: When some females begin hunting, every pride will move to one of the locations of the territory. The first LOA-based phase decides the scope of competition for the fulfilment. The magnitude of this pride's tournament is subsequently determined as follows.

$$T_j^{Size} = \max\left(2.ceil\left(\frac{K_j(s)}{2}\right)\right) \quad (28)$$

Where, $(K_j(s))$ is the percentage of lions in the population j that have improved their physical fitness since the previous iteration. The following phase uses the tournament choice to shift each female in pride to a location outside that pride's region.

Step 2.3 - Roaming: The wandering method is an intense neighbourhood search that reinforces a recommended method's ability to uncover and improve solutions. The best location is modified if required, and Lion is set to the most recently best-visited position.

Step 2.4 - Mating: According to LOA, %Ma of a pride's female lions mate with one or more local males, each chosen randomly for giving birth to cubs. Every mating activity leads to the delivery of two new offspring based on the subsequent equations:

$$Offspring1 = \beta \times Female\ Lion + \sum \frac{(1-\beta)}{\sum_{i=1}^{NR} S_i} \times Male\ Lion \times S_i \quad (29)$$

$$Offspring2 = (1 - \beta) \times Female\ Lion + \sum \frac{\beta}{\sum_{i=1}^{NR} S_i} \times Male\ Lion \times S_i \quad (30)$$

Where, β is a randomized number with a standard deviation of 0.1 and a mean of 0.5. If male i is chosen for mating, the value is 1; else, it is 0, and NR represents the total number of permanent men in the prides.

Step 2.5 - Defense: Males in the pride who are new and experienced are going to battle. Males lacking in power are going to give up their satisfaction and flee. With the help of this strategy, this method can keep mighty male lions as LOA solutions. The proposed LOA optimally tune the parameter of the ANFIS controller, which provides stabilized DC-link voltage with the effectual working functionality of a PV-wind system.

### 3.5. 31 Level CHB MLI Modelling

MLI is frequently employed in medium to high power requirements. Cascaded H-Bridge (CHB) is a unique MLI type. The CHB inverter is favoured in these configurations because of its straightforward design, versatility, and capacity to deal with clean energy sources. The size of the DC voltage source distinguishes asymmetrical and symmetrical CHB inverters.

As seen in Figure 7, the voltage from the source in a symmetric CHB MLI has the same amplitude. If "N" linked H-bridges exist, the resultant voltage can reach "M" levels, where M=2N+1 is the total number of levels. Consequently, a symmetrical CHB MLI employs fifteen H-bridges to generate a 31-level output voltage waveform. An asymmetrical CHB MLI requires eight MOSFET switches and four power diodes to generate a 31-level output waveform. As an outcome, asymmetrical designs are preferable since they need fewer elements to provide higher peak voltage levels. Therefore, switching losses are significantly reduced. Here, the inverter output voltage is shown in Table 1. The logical gate circuit accepts sine, and DC offset waveforms and converts them into pulses of switching for gates that generate PWM for the switches.

Table 1. Switching table of 31-level CHB MLI

Inverter V_{output}	S_4	S_3	S_2	S_1	H_1	H_2	H_3	H_4
15 V_{dc}	1	1	1	1	1	1	0	0
14 V_{dc}	1	1	1	0	1	1	0	0
13 V_{dc}	1	1	0	1	1	1	0	0
12 V_{dc}	1	1	0	0	1	1	0	0
11 V_{dc}	1	0	1	1	1	1	0	0
10 V_{dc}	1	0	1	0	1	1	0	0
9 V_{dc}	1	0	0	1	1	1	0	0
8 V_{dc}	1	0	0	0	1	1	0	0
7 V_{dc}	0	1	1	1	1	1	0	0
6 V_{dc}	0	1	1	0	1	1	0	0
5 V_{dc}	0	1	0	1	1	1	0	0
4 V_{dc}	0	1	0	0	1	1	0	0
3 V_{dc}	0	0	1	1	1	1	0	0
2 V_{dc}	0	0	1	0	1	1	0	0
1 V_{dc}	0	0	0	1	1	1	0	0
0 V_{dc}	0	0	0	0	0	0	0	0
-1 V_{dc}	0	0	0	1	0	0	1	1
-2 V_{dc}	0	0	1	0	0	0	1	1
-3 V_{dc}	0	0	1	1	0	0	1	1
-4 V_{dc}	0	1	0	0	0	0	1	1
-5 V_{dc}	0	1	0	1	0	0	1	1
-6 V_{dc}	0	1	1	0	0	0	1	1
-7 V_{dc}	0	1	1	1	0	0	1	1
-8 V_{dc}	1	0	0	0	0	0	1	1
-9 V_{dc}	1	0	0	1	0	0	1	1
-10 V_{dc}	1	0	1	0	0	0	1	1
-11 V_{dc}	1	0	1	1	0	0	1	1
-12 V_{dc}	1	1	0	0	0	0	1	1
-13 V_{dc}	1	1	0	1	0	0	1	1
-14 V_{dc}	1	1	1	0	0	0	1	1
-15 V_{dc}	1	1	1	1	0	0	1	1

Fig. 7 31-level CHB MLI

Fig. 8 Bidirectional DC-DC converter
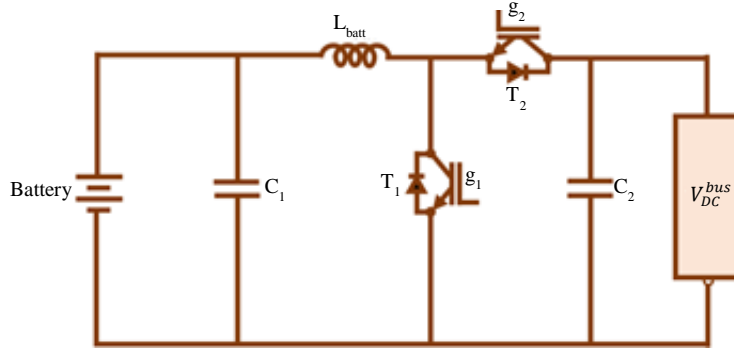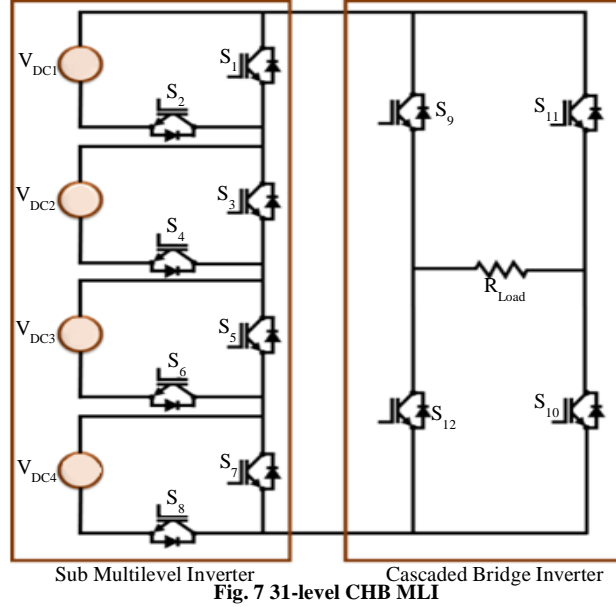
3.6. Bidirectional DC-DC Converter for Battery

The bidirectional circulation of electrical energy is essential for energy conversion in the Battery system. The DC/DC current reversing chopper is employed in the control system to achieve this goal. Figure 8 depicts the structure of the converter under consideration. The DC/DC converter is made up of two regulated switches, Sa and Sb, as well as an inductor Ld, and a filter capacitor Cd. The converter is a hybrid of two fundamental chopper circuits: a step-down and a step-up chopper. The bidirectional DC/DC converter allows for power mode operation when recharging the battery and regeneration mode function while draining the battery. It is generated by a proper control system, which creates two control signals for the converter's two controlled transistor switches.

3.7. Modelling of 3φ Induction Motor

In an equilibrium situation, the three-phase voltage at the stator of an IM can be described as;

$$V_x = \sqrt{2V_{rms}} \sin(\omega t) \tag{31}$$

$$V_y = \sqrt{2V_{rms}} \sin\left(\omega t - \frac{2\pi}{3}\right) \tag{32}$$

$$V_z = \sqrt{2V_{rms}} \sin\left(\omega t + \frac{2\pi}{3}\right) \tag{33}$$

The three balanced voltages above are transferred into the dqo axis's two-phase consecutively rotating reference frame. This is performed by employing the subsequent equation:

$$\begin{bmatrix} v_\alpha \\ v_\beta \end{bmatrix} = \frac{2}{3} \begin{bmatrix} 1 & 1/2 & -1/2 \\ 0 & \sqrt{3}/2 & -\sqrt{3}/2 \end{bmatrix} \begin{bmatrix} v_a \\ v_b \\ v_c \end{bmatrix} \tag{34}$$

Following that, the dq axis voltages are determined,

$$\begin{bmatrix} v_d \\ v_q \end{bmatrix} = \begin{bmatrix} \cos\theta & \sin\theta \\ -\sin\theta & \cos\theta \end{bmatrix} \begin{bmatrix} v_\alpha \\ v_\beta \end{bmatrix} \tag{35}$$

The following formula is used to calculate the instantaneous value of a three-phase IM's rotor and stator currents;

$$\begin{bmatrix} i_\alpha \\ i_\beta \end{bmatrix} = \begin{bmatrix} \cos\theta & -\sin\theta \\ \sin\theta & \cos\theta \end{bmatrix} \begin{bmatrix} i_d \\ i_q \end{bmatrix} \tag{36}$$

$$\begin{bmatrix} v_a \\ v_b \\ v_c \end{bmatrix} = \frac{2}{3} \begin{bmatrix} 1 & 0 \\ 1/2 & -\sqrt{3}/2 \\ -1/2 & -\sqrt{3}/2 \end{bmatrix} \begin{bmatrix} i_\alpha \\ i_\beta \end{bmatrix} \tag{37}$$

Both direct and quadrature (dq) rotor and stator power calculations of an IM are outlined below:

$$V_{qs} = R_s i_{qs} + \frac{d}{dt}\psi_{qs} + \omega_e \psi_{ds} \tag{38}$$

$$V_{ds} = R_s i_{ds} + \frac{d}{dt}\psi_{ds} - \omega_e \psi_{qs} \tag{39}$$

$$V_{qr} = R_r i_{qr} + \frac{d}{dt}\psi_{qr} + (\omega_e - \omega_r)\psi_{dr} \tag{40}$$

$$V_{dr} = R_r i_{dr} + \frac{d}{dt}\psi_{qr} - (\omega_e - \omega_r)\psi_{qr} \tag{41}$$

In this case, $\_\psi_{qr}, \psi_{dr}$ and ψ_{qs}, ψ_{ds} are indicated as d and q axis connections for rotor and stator flux, and the formulae are $\_\omega_e - \omega_r, \omega_e\psi_{qs}, (\omega_e - \omega_r)\psi_{dr}$, and $(\omega_e - \omega_r)\psi_{qr}$ in rotating types, and the rotor revolves at r speed. The rotor voltages V_{dr} and V_{dr} are zero since the rotating cage bars are shorted. As a consequence, the flux linkage formula appears to be the following:

$$\frac{d\psi_{qs}}{dt} = \omega_b \left[v_{qs} - \frac{\omega_e}{\omega_b}\psi_{ds} + \frac{R_s}{Xl_s}(\psi_{mq} - \psi_{qs}) \right] \tag{42}$$

$$\frac{d\psi_{ds}}{dt} = \omega_b \left[v_{ds} + \frac{\omega_e}{\omega_b}\psi_{qs} + \frac{R_s}{Xl_s}(\psi_{md} - \psi_{ds}) \right] \tag{43}$$

$$\frac{d\psi_{qr}}{dt} = \omega_b \left[v_{qs} - \left(\frac{\omega_e - \omega_r}{\omega_b}\right)\psi_{dr} + \frac{R_r}{Xl_r}(\psi_{mq} - \psi_{qr}) \right] \tag{44}$$

$$\frac{d\psi_{dr}}{dt} = \omega_b \left[v_{dr} + \left(\frac{\omega_e - \omega_r}{\omega_b}\right)\psi_{qr} + \frac{R_r}{Xl_r}(\psi_{md} - \psi_{dr}) \right] \tag{45}$$

Where,

$$\psi_{mq} = X_{ml} \left[\frac{\psi_{qs}}{X_{ls}} + \frac{\psi_{qr}}{X_{lr}} \right] \tag{46}$$

$$\psi_{md} = X_{ml} \left[\frac{\psi_{ds}}{X_{ls}} + \frac{\psi_{dr}}{X_{lr}} \right] \tag{47}$$

$$X_{ml} = \frac{1}{\left(\frac{1}{X_m} + \frac{1}{X_{ls}} + \frac{1}{X_{lr}}\right)} \tag{48}$$

The following flux-linked computations are used to calculate current:

$$i_{qs} = \frac{1}{X_{ls}}(\psi_{qs} - \psi_{mq}) \tag{49}$$

$$i_{ds} = \frac{1}{X_{ls}}(\psi_{ds} - \psi_{md}) \tag{50}$$

$$i_{qr} = \frac{1}{X_{ir}}(\psi_{qr} - \psi_{mq}) \tag{51}$$

$$i_{dr} = \frac{1}{X_{lr}}(\psi_{dr} - \psi_{md}) \tag{52}$$

As a consequence, both torque and speed are computed as follows.

$$T_e = \frac{3}{2}\left(\frac{P}{2}\right)(\lambda_{qr} i_{dr} - \lambda_{dr} i_{qr}) \tag{53}$$

$$\omega_r = \int \frac{p}{2J}(T_e - T_L) \tag{54}$$

When determining the torque and speed equation in the configuration of dq flux linkage and stator current configuration, the dq axis conversion ought to be connected to the machine input (stator) voltage, where J: is the inertia moment and p is the number of poles. Utilizing a PI controller, the speed of a three-phase induction motor is governed.

4. Results and Discussion

This work's primary objective is to develop a maritime propulsion system that uses clean energy sources. A high-gain SEPIC converter aims to deliver a steady, ripple-free output voltage. A PI controller controls the rate of motion of an induction motor.

Under various climatic circumstances, PV and wind systems' performance is increased using Lion-optimized ANFIS controllers. The power supply to the three-phase IMs is stabilized and fluctuation-free due to the 31-level CHB MLI. Through speed control testing and MATLAB simulation, the efficacy of the IM is assessed. Parametric descriptions of the proposed system and 3ϕ IM are illustrated in Tables 2 and 3.

Figure 9 illustrates the simulation outcomes for the temperature waveform and solar irradiance waveform acquired using the Matlab programme. The temperature waveform proves unequivocally that the solar panel's temperature is constant at 25°C for the first 0.3 seconds. After that, the temperature is abruptly increased and kept at 35°C for 0.3 seconds. Similarly, the solar irradiation is held at 800W/sqm for 0.3 seconds before rapidly increasing to 1000W/sqm and remaining constant afterwards.

Table 2. Parameter descriptions of the proposed system

PV-DFIG	
Parameter	**Values**
Open Circuit Voltage	12V
Peak Power	10kW
Series Connected Solar Panel	36
No. of Turbine	1
Voltage	575V
Switching Frequency	10kHz
Power	10kW
High-Gain SEPIC Converter	
Parameter	**Values**
L_1, L_2	1mH
L_3, L_0	3.7mH
C_1, C_2	47μF
C_o	570μF
Diode	IN4148
Switch	IRF840

Table 3. Parameter description of induction motor

3ϕ Induction Motor	
Parameters	**Values**
Power	1Hp
Speed	1390 rpm
Voltage	415V (AC)
No. of Poles	4
Frequency	50 Hz
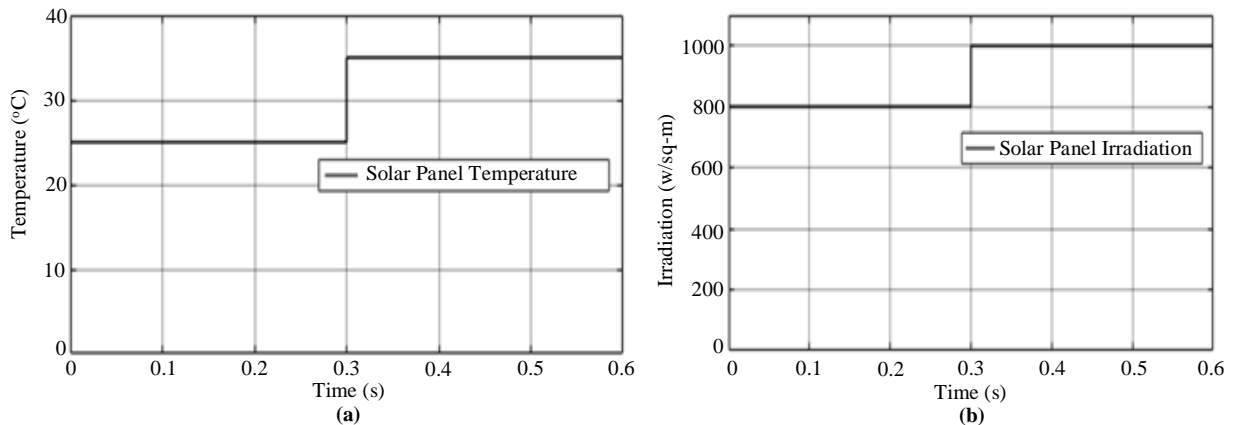
Fig. 9 Solar panel (a) Temperature, and (b) Irradiation waveforms.
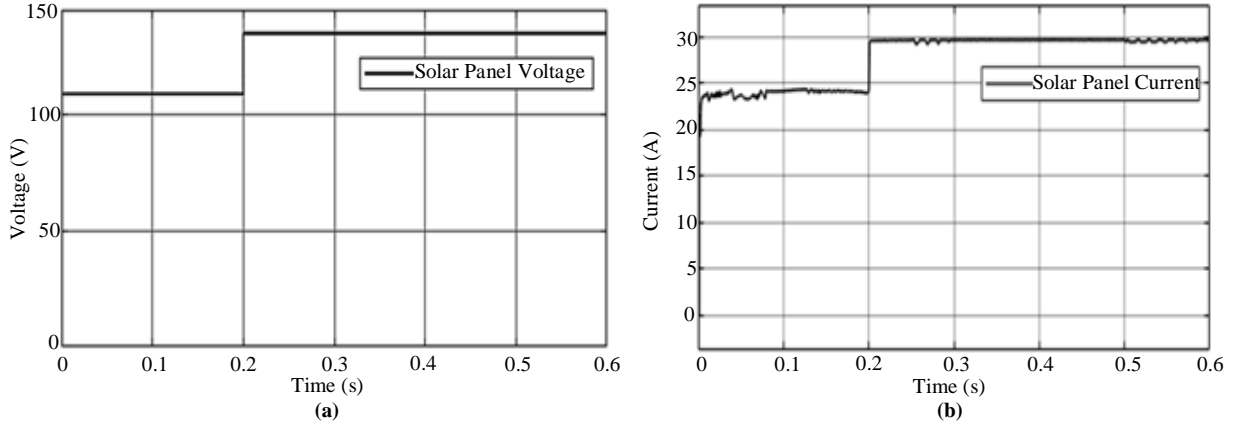
Fig. 10 Solar panel output (a) Voltage, and (b) Current waveforms.
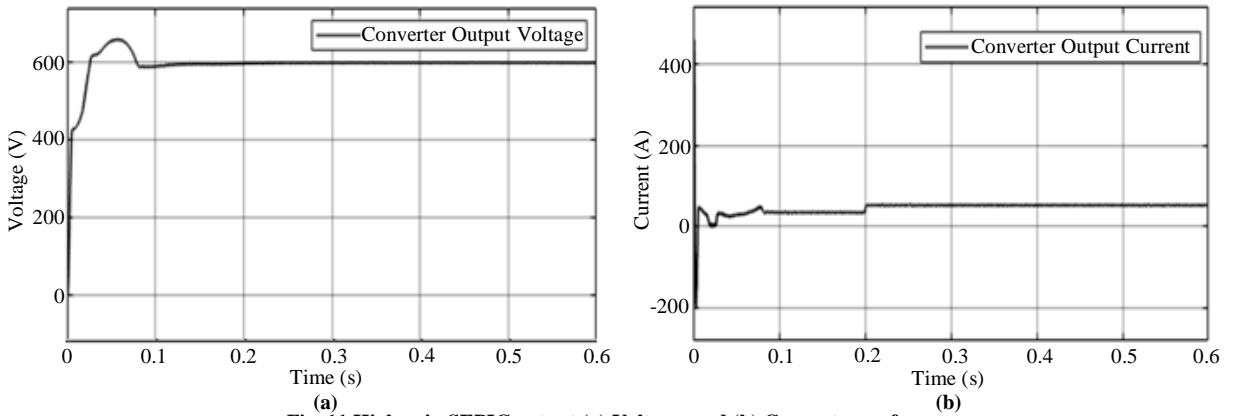
Fig. 11 High gain SEPIC output (a) Voltage, and (b) Current waveforms.

The solar panel output current and voltage waveform are illustrated in Figure 10. From the waveform observation, it is observed that the constant current and voltage values of 110V & 30A are maintained, respectively. Figure 11 shows the High Gain SEPIC converter's output voltage and current waveforms. The converter's resultant voltage and current waveform show that a steady current of 600 V remains stable at 0.1 second and a voltage of 30 A. DFIG output voltage waveforms are displayed in Figure 12(a). As seen in Figure 12(b), a PWM rectifier preserves the DFIG output uninterrupted disruption and delivers the best result possible.

For 0.1s, the DFIG output increases. Using the recommended Lion-optimized ANFIS mechanism, the initial discrepancies in a DC-link voltage are managed, and a constant DC-link voltage of 600V is retained.

A DC bus voltage change in photovoltaic energy production maintains a constant voltage of 120 V, as indicated in Figure 13(a).In the initial case, the battery current varies but remains constant at 1.6 amps, as indicated in Figure 13(b). The battery fills the power gap and keeps a battery's level of charge at 60%, as shown in Figure 13(c).
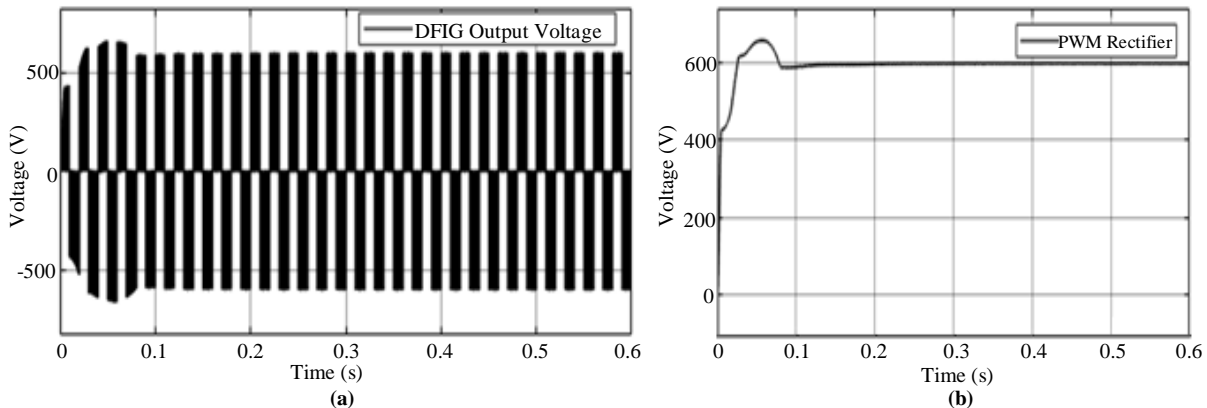

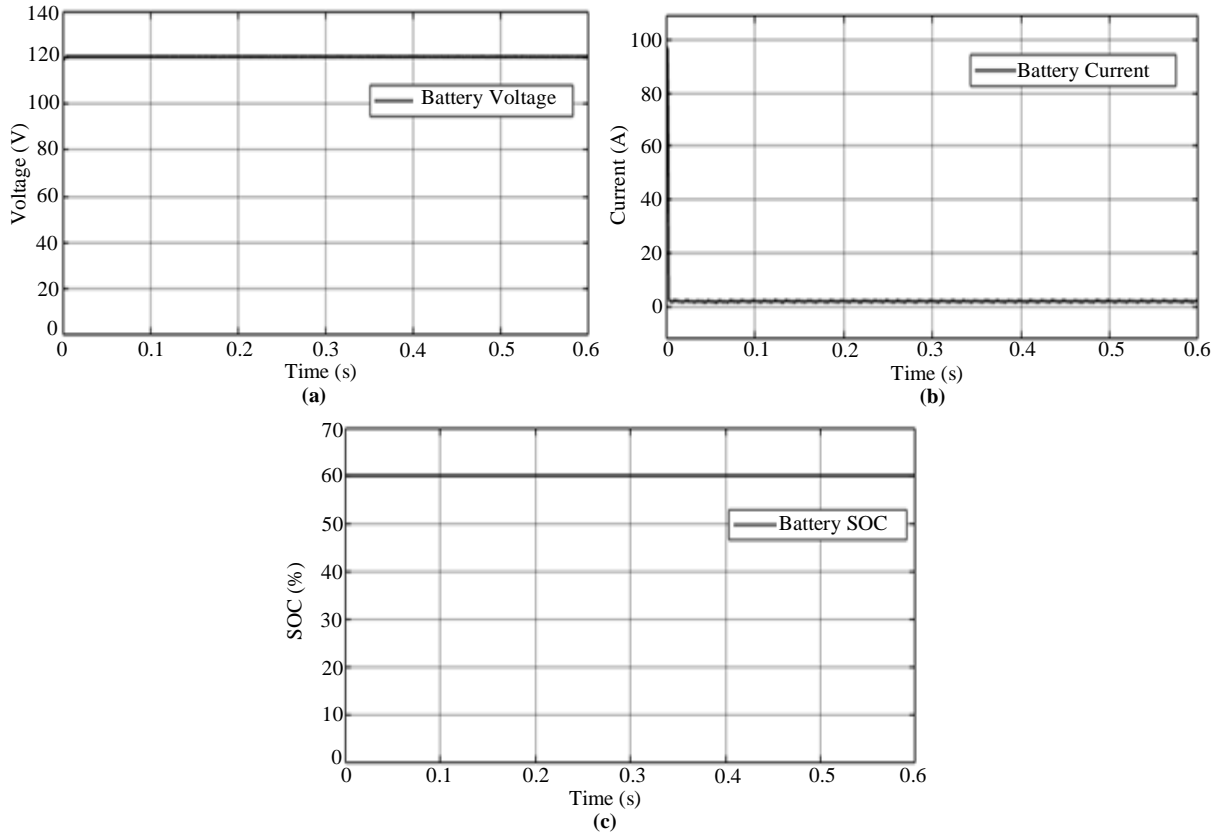**Fig. 12 WECS output (a) DFIG voltage, and (b) PWM rectifier voltage waveforms.**

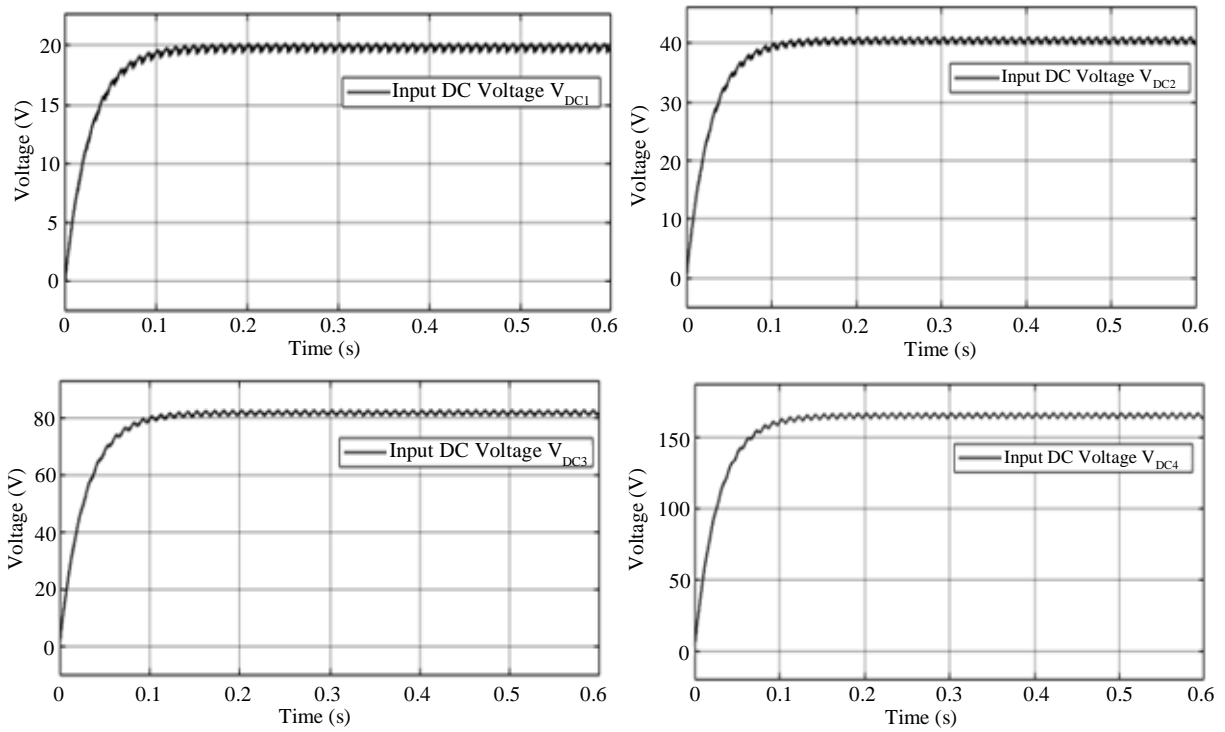**Fig. 13 Battery output waveforms (a) Voltage, (b) Current, and (c) SOC waveforms.**

Fig. 14 Waveforms of input DC voltage levels

The input in different dc levels of waveforms is demonstrated in Figure 14. From the waveform observation, at V_{DC1}, V_{DC2} level, the constant 20V and 40V is obtained with small distortions. Likewise, V_{DC3}, V_{DC4} levels, the stable 80V and 160V, are kept preserved with a minimal amount of fluctuations.

Figure 15 indicates the resultant voltage waveform of 31-level CHB MLI, which shows a steady and consistent voltage of 300 V. Similarly, the constant current 6 A is preserved after 0.2 sec.

Figure 16 illustrates the resulting real and reactive power, and the amount of reactive power is determined to be small. In Figure 17(a), the torque amplitude of the three-phase IM is displayed. The torque waveform demonstrates that applying PI reduces variations in the beginning phase

and maintains it at 0.3 seconds. Rotor angle is the amount of rotation or positional shift a rotor makes in relation to an angle measuring, as indicated in Figure 17 b). Likewise, the enhanced power factor is obtained in Figure 17(c).

Figure 18 shows the direct and quadrature (dq) axes waveforms of an induction motor's rotor and stator. Figure 19(a) demonstrates that the PI initiates the speed control in 0.3 seconds; this controller achieves a steady speed of 2000 rpm, and Figure 19(b) displays the desired consistent speed of 2500 rpm.

Figure 20 shows the proposed system's present THD waveform, which shows the amount of harmonics present. It is noted that a minimized THD value of 2.33% is attained, which is minimal and complies with the standards of the IEEE519 standard.
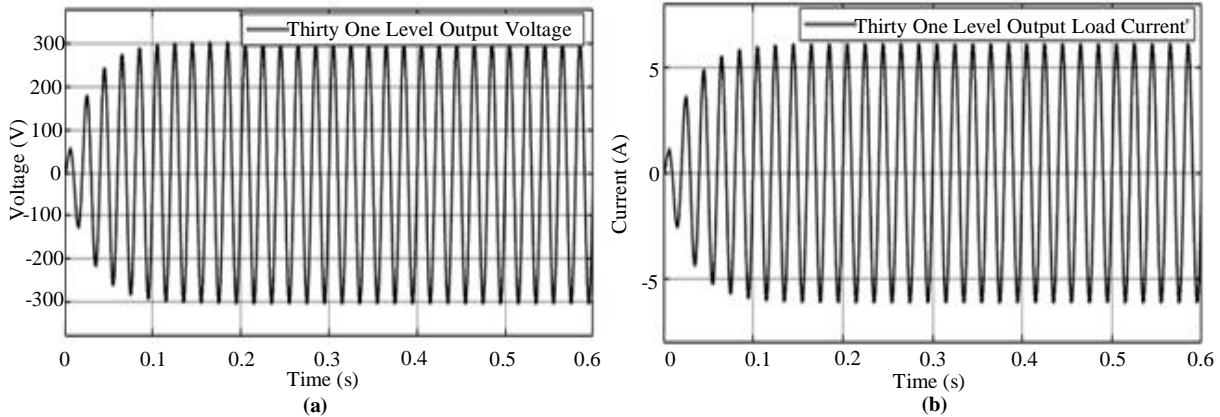

(a) **(b)**
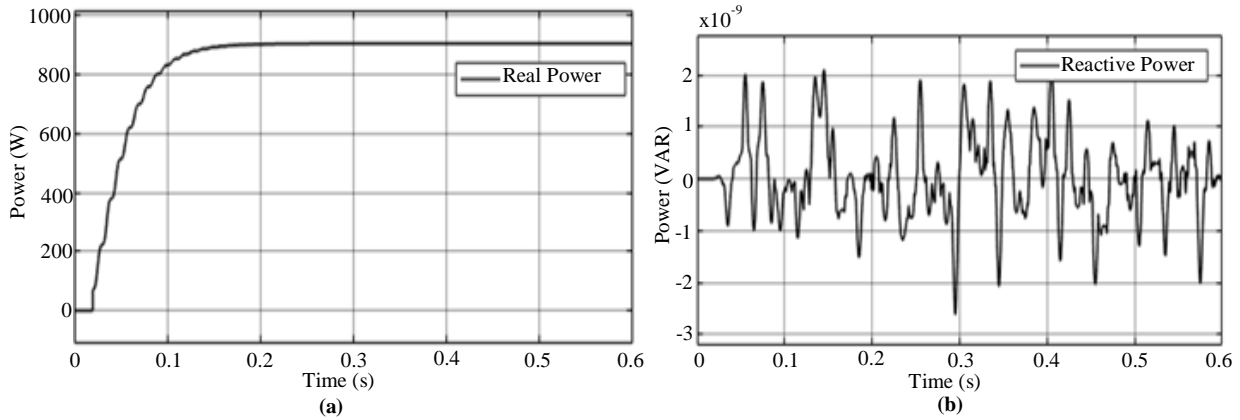**Fig. 15 Waveforms of 31-level CHB MLI (a) Voltage, and (b) Current.**

(a) **(b)**
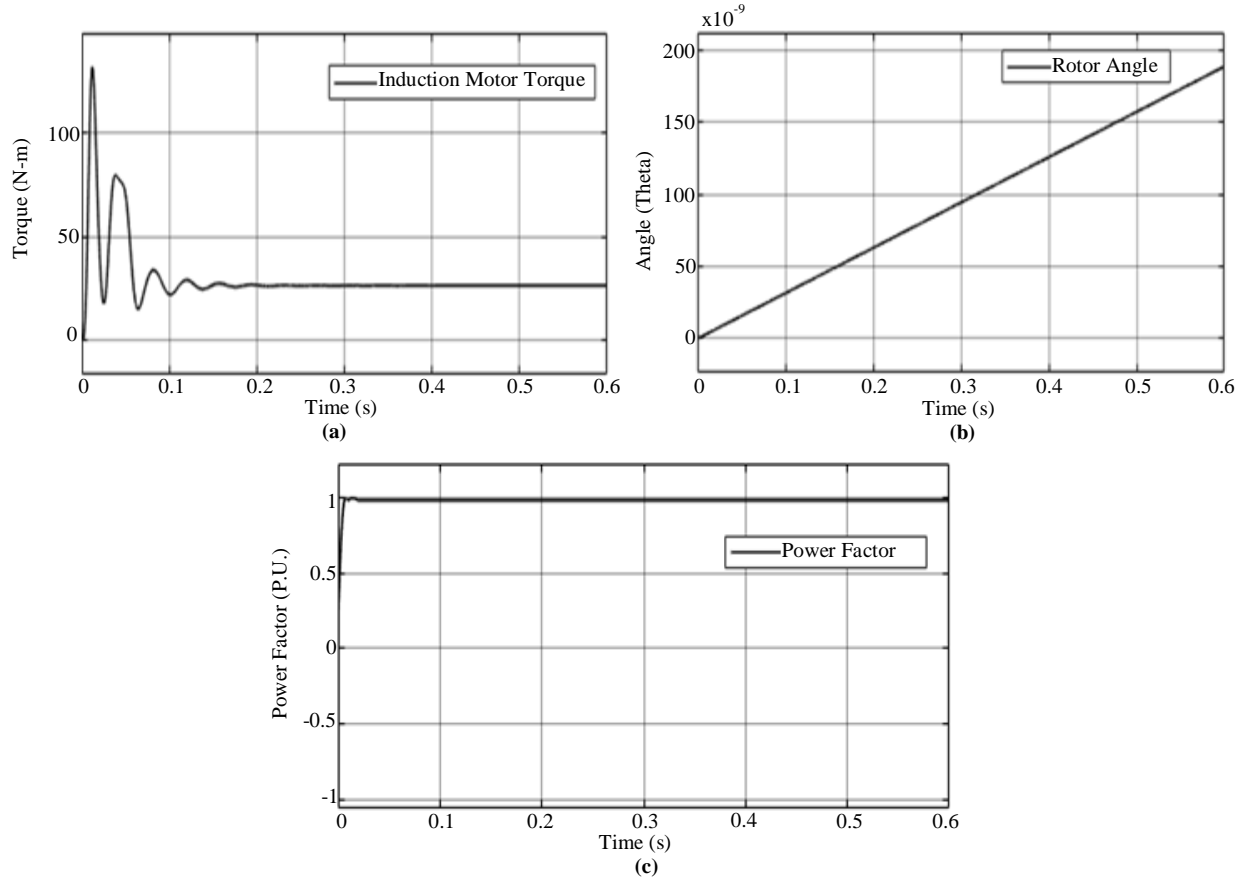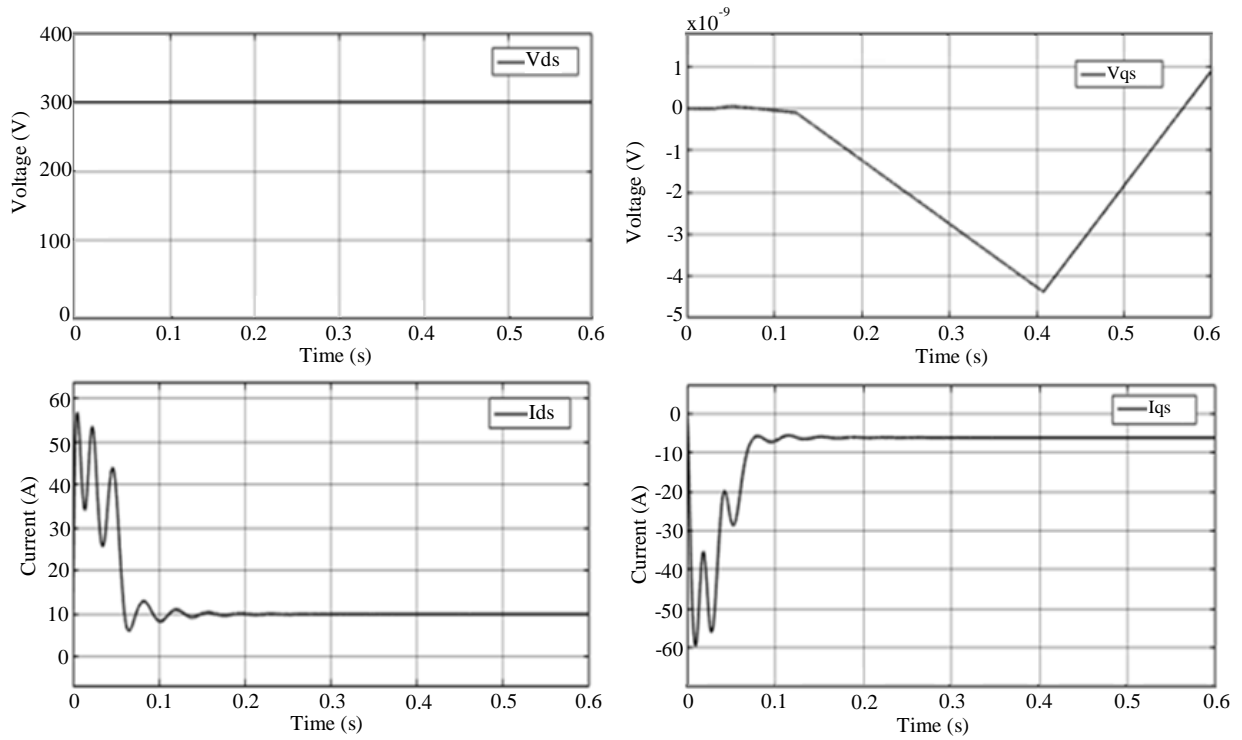**Fig. 16 Waveforms illustrating (a) Real power, and (b) Reactive power.**

Fig. 17 Waveforms illustrating (a) IM torque, (b) Rotor angle, and (c) Power factor.
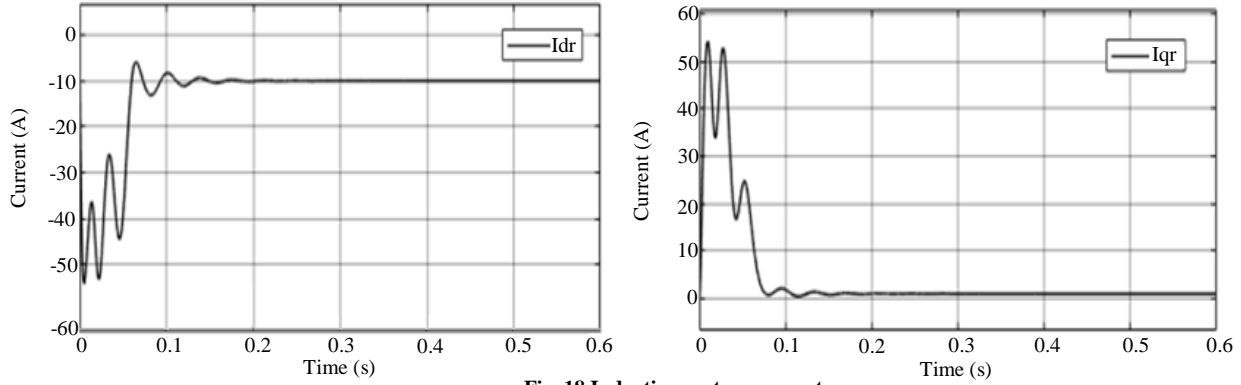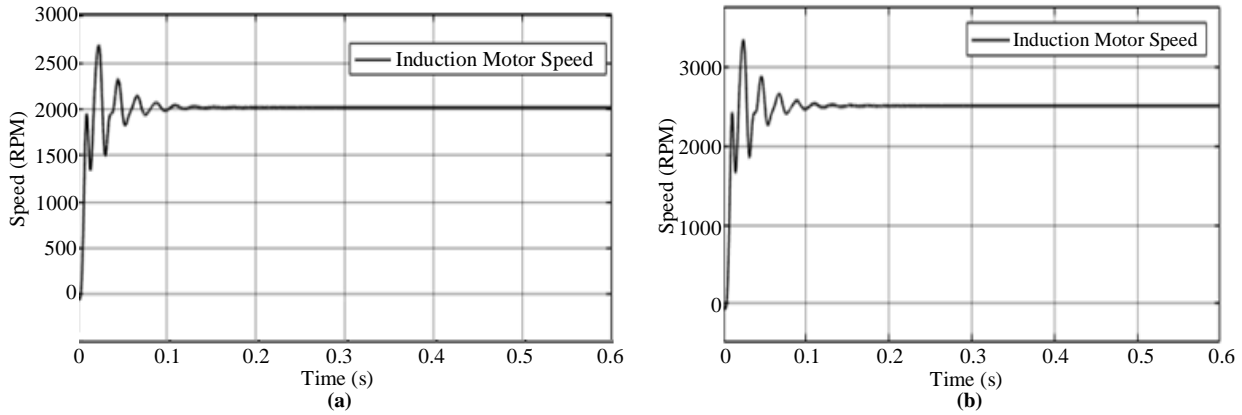
Fig. 18 Induction motor parameters

Fig. 19 Induction motor speed (a) At 2000 rpm, and (b) At 2500 rpm.
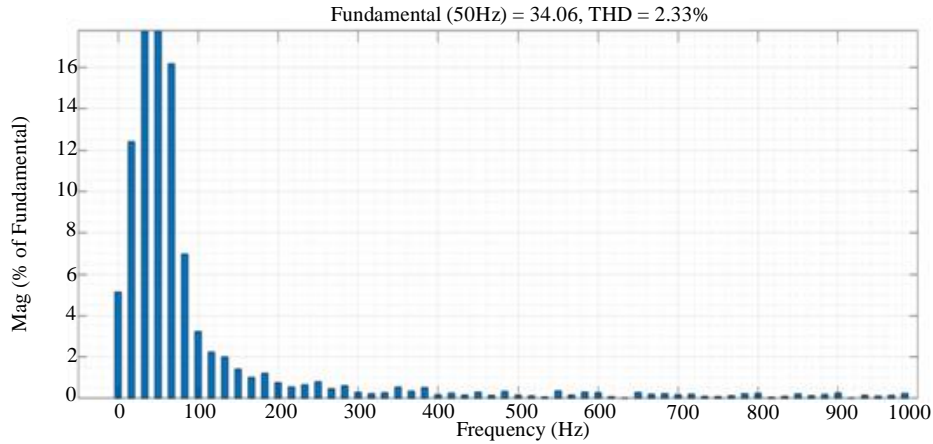

Fig. 20 THD waveform

4.1. Comparison Analysis

The High gain SEPIC converter efficiency is compared to other existing converters to assess that the proposed converters perform better in enhancing PV system reliability. When contrasted to other converters, the proposed high gain SEPIC has an exceptional efficiency of 95.6%, which is shown in Figure 21. Figure 22 depicts THD comparison of 31-level CHB MLI with the other CHB MLI including 5 level [21],7- level [21] 11-level [21] and 13 level CHB MLI is presented. The graph reveals that the proposed 31-level CHB MLI has a minimized THD value of 2.33%. Similarly, Table 4 compares the controller's dynamic response; based on the table values, the proposed Lion-optimized ANFIS controller has a quick settling time value of 0.15s.
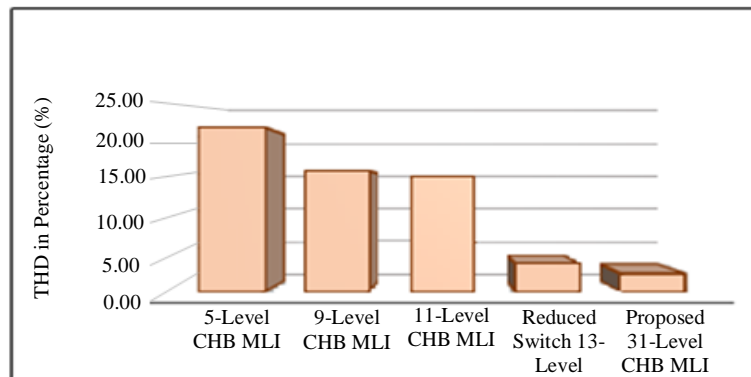
Table 4. Efficiency comparison of converters

Converters	Efficiency (%)
Boost	80 [18]
Cuk	85 [19]
SEPIC	88.82 [20]
High Gain SEPIC	95.6
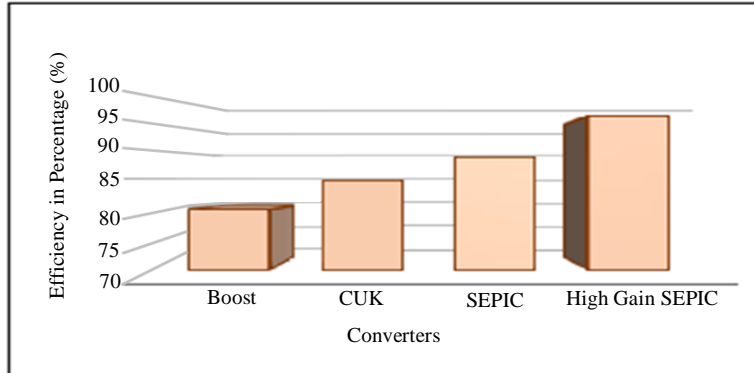
Fig. 21 Efficiency comparison

Table 5. THD comparison of Multi-Level Inverters

MLI Topology	THD %
5-Level CHB MLI	20.64
9-Level CHB MLI	15.17
11-Level CHB MLI	14.44
Reduced Switch 13-Level	3.54
Proposed 31-Level CHB MLI	2.33

Fig. 22 THD comparison

Table 6. Dynamic response comparison

Controllers	Rise Time t_r	Peak Time t_p	Settling Time t_s
PSO-FUZZY controller	0.4	0.2	0.56
PSO-ANN controller	0.3	0.18	0.43
PSO-ANFIS controller	0.29	0.15	0.32
Lion-ANFIS controller	0.08	0.04	0.15s

5. Conclusion

This study proposes a 31-level CHB MLI with Lion Optimised ANFIS Controller for controlling a three-phase IM drive for a maritime propulsion system. This study generates electricity using DFIG-WECS and PV. The work under evaluation boosts PV voltage with a high gain SEPIC and regulates the converter efficiently using a Lion Optimised ANFIS. To ensure adequate control, a PWM rectifier and LA-ANFIS controller convert the AC supply from DFIG-WECS to DC. The converter's output is transformed into free-of-distortion alternating current voltage provided to the motor in maritime propulsion systems using a 31 level CHB MLI. A PI controller is used to regulate three-phase IM speed, which results in outputs with governed speed. According to the simulation findings, the proposed system is significantly more effective than other alternative approaches in terms of efficiency and minimized THD value, with values of 95.6% and 2.33%, respectively.

References

[1] Saman Nasiri et al., "Analysis of All-Electric Ship Motions Impact on PV System Output Power in Waves," *2022 IEEE Transportation Electrification Conference & Expo (ITEC)*, Anaheim, CA, USA, pp. 450-455, 2022. [CrossRef] [Google Scholar] [Publisher Link]

[2] Noor Habib Khan et al., "Adopting Scenario-Based Approach to Solve Optimal Reactive Power Dispatch Problem with Integration of Wind and Solar Energy Using Improved Marine Predator Algorithm," *Ain Shams Engineering Journal*, vol. 13, no. 5, 2022. [CrossRef] [Google Scholar] [Publisher Link]

[3] Jun Hou, Jing Sun, and Heath Hofmann, "Control Development and Performance Evaluation for Battery/Flywheel Hybrid Energy Storage Solutions to Mitigate Load Fluctuations in All-Electric Ship Propulsion Systems," *Applied Energy*, vol. 212, pp. 919-930, 2018. [CrossRef] [Google Scholar] [Publisher Link]

[4] Jun Hou et al., "Implementation and Evaluation of Real-Time Model Predictive Control for Load Fluctuations Mitigation in All-Electric Ship Propulsion Systems," *Applied Energy*, vol. 230, pp. 62-77, 2018. [CrossRef] [Google Scholar] [Publisher Link]

[5] David Torrey et al., "Superconducting Synchronous Motors for Electric Ship Propulsion," *IEEE Transactions on Applied Superconductivity*, vol. 30, no. 4, pp. 1-8, 2020. [CrossRef] [Google Scholar] [Publisher Link]

[6] Alessandro Boveri et al., "Optimal Sizing of Energy Storage Systems for Shipboard Applications," *IEEE Transactions on Energy Conversion*, vol. 34, no. 2, pp. 801-811, 2018. [CrossRef] [Google Scholar] [Publisher Link]

[7] Hamoud Alafnan et al., "Stability Improvement of DC Power Systems in an All-Electric Ship Using Hybrid SMES/Battery," *IEEE Transactions on Applied Superconductivity*, vol. 28, no. 3, pp. 1-6, 2018. [CrossRef] [Google Scholar] [Publisher Link]

[8] Deepak Ronanki, and Sheldon S. Williamson, "A Simplified Space Vector Pulse Width Modulation Implementation in Modular Multilevel Converters for Electric Ship Propulsion Systems," *IEEE Transactions on Transportation Electrification*, vol. 5, no. 1, pp. 335-342, 2018. [CrossRef] [Google Scholar] [Publisher Link]

[9] Pourya Ojaghlu, and Abolfazl Vahedi, "Specification and Design of Ring Winding Axial Flux Motor for Rim-Driven Thruster of Ship Electric Propulsion," *IEEE Transactions on Vehicular Technology*, vol. 68, no. 2, pp. 1318-1326, 2019. [CrossRef] [Google Scholar] [Publisher Link]

[10] Jing Zhou et al., "A Fault Detection and Health Monitoring Scheme for Ship Propulsion Systems Using SVM Technique," *IEEE Access*, vol. 6, pp. 16207-16215, 2018. [CrossRef] [Google Scholar] [Publisher Link]

[11] Amirhossein Dolatabadi, and Behnam Mohammadi-Ivatloo, "Stochastic Risk-Constrained Optimal Sizing for Hybrid Power System of Merchant Marine Vessels," *IEEE Transactions on Industrial Informatics*, vol. 14, no. 12, pp. 5509-5517, 2018. [CrossRef] [Google Scholar] [Publisher Link]

[12] Abba Lawan Bukar et al., "Optimal Planning of Hybrid Photovoltaic/Battery/Diesel Generator in Ship Power System," *International Journal of Power Electronics and Drive Systems*, vol. 11, no. 3, pp. 1527-1535, 2020. [CrossRef] [Google Scholar] [Publisher Link]

[13] Hang Zhao et al., "Design and Optimization of a Magnetic-Geared Direct-Drive Machine with V-Shaped Permanent Magnets for Ship Propulsion," *IEEE Transactions on Transportation Electrification*, vol. 8, no. 2, pp. 1619-1633, 2022. [CrossRef] [Google Scholar] [Publisher Link]

[14] Javad Khazaei, "Optimal Flow of MVDC Shipboard Microgrids with Hybrid Storage Enhanced with Capacitive and Resistive Droop Controllers," *IEEE Transactions on Power Systems*, vol. 36, no. 4, pp. 3728-3739, 2021. [CrossRef] [Google Scholar] [Publisher Link]

[15] Arshiah Yusuf Mirza, and Ali M. Bazzi, "Effects of 7-Level ANPC SiC Inverter on Motor Stator Insulation and Cable Insulation in an Electric Ship Propulsion Drive," *2021 IEEE Electric Ship Technologies Symposium (ESTS)*, Arlington, VA, USA, pp. 1-4, 2021. [CrossRef] [Google Scholar] [Publisher Link]

[16] Yongchao Han, and Ming Li, "Nonlinear Dynamic Characteristics of Marine Rotor-Bearing System under Heaving Motion," *Shock and Vibration*, vol. 2019, pp. 1-16, 2019. [CrossRef] [Google Scholar] [Publisher Link]

[17] Libing Jing et al., "Characteristic Analysis of the Magnetic Variable Speed Diesel–Electric Hybrid Motor with Auxiliary Teeth for Ship Propulsion," *IEEE/ASME Transactions on Mechatronics*, 2023. [CrossRef] [Google Scholar] [Publisher Link]

[18] Farzam Nejabatkhah et al., "Modeling and Control of a New Three-Input DC–DC Boost Converter for Hybrid PV/FC/Battery Power System," *IEEE Transactions on Power Electronics*, vol. 27, no. 5, pp. 2309-2324, 2012. [CrossRef] [Google Scholar] [Publisher Link]

[19] F. Galea et al., "Design of a High Efficiency Wide Input Range Isolated Cuk DC-DC Converter for Grid Connected Regenerative Active Loads," *2011 World Engineers' Convention*, 2011. [Google Scholar] [Publisher Link]

[20] Patan Javeed et al., "SEPIC Converter for Low Power LED Applications," *Journal of Physics: Conference Series*, vol. 1818, 2021. [CrossRef] [Google Scholar] [Publisher Link]

[21] Dodda Satish Reddy et al., "A Comparative Investigation of 5-Level, 9-Level and 11-Level Conventional Cascaded H-Bridge Multilevel Inverters by Using Simulink / Matlab," *International Journal of Research in Engineering & Technology*, vol. 5, no. 7, pp. 19-26, 2017. [Google Scholar] [Publisher Link]